The Astrophysical Journal, 871:123 (15pp), 2019 January 20 https://doi.org/10.3847/1538-4357/aaf564

The Short GRB 170817A: Modeling the Off-axis Emission and Implications on the Ejecta Magnetization

N. Fraija[1], F. De Colle[2], P. Veres[3], S. Dichiara[1,4,5], R. Barniol Duran[6], A. Galvan-Gamez[1], and A. C. Caligula do E. S. Pedreira[1,7]
[1] Instituto de Astronomía, Universidad Nacional Autónoma de México, Circuito Exterior, C.U., A. Postal 70-264, 04510 Cd. de México, México
nifraija@astro.unam.mx
[2] Instituto de Ciencias Nucleares, Universidad Nacional Autónoma de México, Circuito Exterior, C.U., A. Postal 70-264, 04510 Cd. de México, México
[3] Center for Space Plasma and Aeronomic Research (CSPAR), University of Alabama in Huntsville, Huntsville, AL 35899, USA
[4] Department of Astronomy, University of Maryland, College Park, MD 20742-4111, USA
[5] Astrophysics Science Division, NASA Goddard Space Flight Center, 8800 Greenbelt Road, Greenbelt, MD 20771, USA
[6] Department of Physics and Astronomy, California State University, Sacramento, 6000 J Street, Sacramento, CA 95819-6041, USA
[7] Instituto de Matemática, Estatísca e Física, Universidade Federal do Rio Grande, Rio Grande 96203-900, Brasil
Received 2017 December 9; revised 2018 November 26; accepted 2018 November 29; published 2019 January 25

Abstract

The short GRB 170817A, detected by the Fermi Gamma-ray Burst Monitor, orbiting satellites and ground-based telescopes, was the electromagnetic counterpart of a gravitational-wave transient (GW170817) from a binary neutron star merger. After this merger, the γ-ray light curve exhibited a faint peak at $\sim$1.7 s and the X-ray, optical, and radio light curves displayed extended emission that increased in brightness up to $\sim$160 days. In this paper, we show that the X-ray, optical and radio fluxes are consistent with the synchrotron forward-shock model viewed off-axis when the matter in the outflow is parameterized through a power-law velocity distribution. We discuss the origin of the γ-ray peak in terms of internal and external shocks. We show that the γ-ray flux might be consistent with a synchrotron self-Compton reverse-shock model observed at high latitudes. Comparing the best-fit values obtained after describing the γ-ray, X-ray, optical, and radio fluxes with our model, we find that the afterglow and γ-ray emission occurred in different regions and also find evidence to propose that the progenitor environment was entrained with magnetic fields; therefore we argue for the presence of magnetic field amplification in the binary neutron star merger.

Key words: acceleration of particles – gamma-ray burst: individual (GRB 170817A) – ISM: general – magnetic fields – radiation mechanisms: non-thermal

1. Introduction

One of the most fascinating extragalactic events is gamma-ray bursts (GRBs). They are known to exhibit a vast variety of spectral and temporal properties. Based on the standard GRB durations and spectral hardness two kinds of progenitor populations have been amply accepted, short ($T_{90} < 2$ s) and long ($T_{90} > 2$ s) GRBs (for a review, see Zhang & Mészáros 2004; Kumar & Zhang 2015). Although discoveries and subsequent studies of long GRBs (lGRBs) have been marked by many successes, the study of short GRBs (sGRBs) has proven to be much more challenging. Significant advances in sGRBs were achieved with the discovery of the first host galaxies and the observations of multiwavelength afterglows (for reviews, see Nakar 2007; Berger 2014). Several lines of evidence have associated the sGRB progenitors with the merger of compact object binaries comprised of a neutron star binary (NS–NS) or a neutron star-black hole (NS-BH; Eichler et al. 1989; Narayan et al. 1992; Lee et al. 2004, 2005; Lee & Ramirez-Ruiz 2007; Nakar 2007). These progenitors are promising candidates to release gravitational waves (GWs) accompanied by an isotropic optical/infrared counterpart, the so-called kilonova or macronova (Li & Paczyński 1998; Rosswog 2005; Metzger et al. 2010; Kasen et al. 2013; Metzger 2017). Because of neutron-rich ejecta from these progenitors, a kilonova/macronova is produced via radioactive decay of unstable heavy nuclei created in the rapid neutron capture (r-process) nucleosynthesis (Lattimer & Schramm 1974, 1976). In addition, a cocoon emission and a delayed non-thermal radiation in radio wavelengths, originated from the interaction of the merger ejecta with the circumburst medium, are expected from these events (Nakar & Piran 2011; Piran et al. 2013; Hotokezaka & Piran 2015; Lazzati et al. 2017a, 2017b). On the other hand, using two non-spinning magnetized NSs initially separated by 48 km with 1.4 solar masses, Price & Rosswog (2006) presented through simulations the magnetic field evolution in a binary NS merger. The main result is that the corresponding magnetic field, of $\sim 10^{12}$ G, present in an NS can be dramatically amplified by several orders of magnitude after the merger. The magnetic field strength that can be reached during the first milliseconds through Kevin–Helmholtz instabilities and turbulent amplification is much higher than $\sim 10^{15}$ G (Price & Rosswog 2006; Zrake & MacFadyen 2013; Giacomazzo et al. 2009; Obergaulinger et al. 2010). Therefore, a degree of magnetization in the ejecta could be expected in the binary NS merger.

During the last decade, the observation of optical and gamma-ray polarization (e.g., see Mundell et al. 2007, 2013; Steele et al. 2009; Troja et al. 2017a) and models of γ-ray, X-ray, and optical bright peaks, which suggests a stronger magnetic field in the reverse-shock region than in the forward-shock region (Kobayashi 2000; Kobayashi & Zhang 2003; Zhang et al. 2003; Kobayashi et al. 2007; Fraija et al. 2012, 2016b, 2017a; Fraija 2015; Fraija & Veres 2018), have provided overwhelming evidence that some lGRB progenitors are endowed with intense magnetic fields (see, e.g., Usov 1992, and references therein). In the context of sGRBs, Fraija et al. (2016b) proposed that the bright peak exhibited at the

prompt/early-afterglow phase could be correlated with the degree of magnetization present in the jet. In particular, the bright peak presented in the Large Area Telescope (LAT) light curve and interpreted in the reverse-shock context provides compelling evidence that the central engine in GRB 090510 was magnetized, as the magnetic field amplification in the binary NS merger is the most promising candidate.

On the other hand, the transition between the prompt emission and the afterglow is one of the most interesting and least understood phases. The prompt-decay phase is attributed to emission from regions located at high latitudes, i.e., from regions located at viewing angles ($\theta_{\rm obs}$) larger by at least a factor $\theta_j \sim \frac{1}{\Gamma}$ with respect to the line of sight (the curvature effect or high-latitude emission). When this effect is present, after the gamma-ray emission from the observer's line of sight has ceased, the off-axis flux at $\theta_{\rm obs} > \theta_j$ is dramatically suppressed unless the burst is very luminous or viewed from near its edge. Because of the curvature effect, the onset of the afterglow could overlap with the high-latitude emission. Radiation generated at the reverse shock would decay fast due to the angular time delay effect (Kumar & Panaitescu 2000). Once the quickly decaying high-latitude emission is small enough, the afterglow emission can be observed (Rees 1999; Dermer et al. 2000; Granot et al. 2002).

GRB 170817A, the electromagnetic counterpart of the gravitational-wave transient associated with an NS–NS coalescence (GW170817; Abbott et al. 2017a, 2017b), was detected by the Gamma-ray Burst Monitor (GBM) on board the *Fermi Gamma-ray Space Telescope* at 12:41:06 UTC, 2017 August 17 (Goldstein et al. 2017). Promptly, this burst was monitored in several electromagnetic bands by multiple ground-based telescopes and satellites (see, e.g., Abbott et al. 2017b, and references therein). By considering the low luminosity observed in GRB 170817A the γ-ray flux has been associated with different emission mechanisms (Bromberg et al. 2017; Gottlieb et al. 2017; Kathirgamaraju et al. 2017, 2018; Kisaka et al. 2017; Fraija et al. 2018) and the X-ray, optical, and radio afterglow with synchrotron forward-shock models when the relativistic jet viewed off-axis and/or cocoon are decelerated in a homogeneous low-density medium $\sim 10^{-5}$–10^{-2} cm^{-3} (Alexander et al. 2017; Granot et al. 2017; Guidorzi et al. 2017; Ioka & Nakamura 2017; Kasliwal et al. 2017; Lazzati et al. 2017c; Margutti et al. 2017a; Mooley et al. 2017; Murguia-Berthier et al. 2017; Piro & Kollmeier 2017; Wang & Huang 2018).

In this paper, we present a comprehensive analysis and description of the short GRB 170817A, in the context of an off-axis jet, when the matter in the outflow is parameterized through a power-law velocity distribution. The paper is arranged as follows. In Section 2, a brief description of multiwavelength observations and GBM data reduction are presented. In Section 3, we model the non-thermal multi-wavelength observations in GRB 170817A and discuss the implications on the ejecta magnetization and conclusions are given in Section 4.

2. GRB 170817A

2.1. Multiwavelength Upper Limits and Observations

GRB 170817A was detected by the GBM-*Fermi* Telescope at 12:41:06 UTC, 2017 August 17 (Goldstein et al. 2017; von Kienlin et al. 2017). This detection was consistent with a gravitational-wave transient observed by LIGO and Virgo observatories. This observational transient was associated with an NS–NS coalescence with a merger time 12:41:04 UTC ~ 2 s before the GBM trigger (Abbott et al. 2017a, 2017b). Immediately afterward, an exhaustive multi-wavelength campaign was launched in order to look for an isotropic electromagnetic counterpart in the optical and infrared bands (see, e.g., Coulter et al. 2017, and references therein). A bright transient in the optical *i*-band with magnitude $m_i = 17.057 \pm 0.0018$ was observed by the 1 m Swope telescope at Las Campanas Observatory in Chile at 10.87 hr (August 17 at 23:33 UTC) after the GMB trigger and afterward during the following 12 hr by multiple ground-based and orbiting optical/IR telescopes. In addition, linear polarization in optical bands was reported, revealing the geometry of the emitting region. This transient was located coming from the center of the galaxy NGC 4993 at a distance of 40 Mpc.

Distinct X-ray observations were carried out by several orbiting satellites for the following eight days without any detection but providing constraining limits (i.e., see Margutti et al. 2017a). From the 9th up to 256th day after the merger, X-ray detections were reported by the *Chandra* and *XMM-Newton* observatories (Troja et al. 2017b; Alexander et al. 2018; D'Avanzo et al. 2018; Margutti et al. 2018). Optical observations and upper limits collected with the Advanced Camera for Surveys Wide Field Camera on board the *Hubble Satellite Telescope* (*HST*), were performed $\sim$100 days after the trigger (Alexander et al. 2018; Lyman et al. 2018; Margutti et al. 2018). On the 16th day after the post-trigger and for more than seven months, the radio counterpart at 3 and 6 GHz was obtained by Very Large Array (VLA; Abbott et al. 2017b; Hallinan et al. 2017; Mooley et al. 2017; Dobie et al. 2018).

2.2. GBM Data Reduction

Event data files were obtained using the GBM trigger time for GRB 170817A 04:47:43 UT on 2017 August 17 (Ackermann et al. 2013; von Kienlin et al. 2017). *Fermi*-GBM data in the energy range of 10–1000 keV were reduced using the public database at the *Fermi* website[8] and the position of this burst is found to be at the coordinates (J2000) R.A. $= 176.^{\circ}8$, decl. $= -39.^{\circ}8$, with an error circle of radius $11.^{\circ}6$. No other sources in the LAT catalog or background emission are considered due to the duration of the event.

Flux values are derived using the spectral analysis package RMfit, version 432.[9] To analyze the signal we use the time-tagged event files of the three triggered Na I detectors n_1, n_2, and n_5. Different spectral models are used to fit the spectrum over different duration periods. Each time bin is chosen by adopting a trade-off between the minimum signal needed to derive a spectrum and the minimum resolution required to preserve the shape of the time evolution. The Comptonized (a power law with exponential cutoff, hereafter referred as CPL) and the simple power-law (PL) functions are used to fit the spectrum up to 0.448 s around the GBM trigger time. The spectral analysis during the time interval [−0.320 s, 0.448 s] after the trigger is reported in Table 1. This table shows the time interval (column one), spectral model (column 2), spectral index (column three), energy peak (column four), temperature of the blackbody (BB) function, and the C-Stat/dof test (last

[8] http://fermi.gsfc.nasa.gov/ssc/data
[9] https://fermi.gsfc.nasa.gov/ssc/data/analysis/rmfit/

Table 1
Spectral Analysis with GBM Data

Time Interval (s)[a]	Model[b]	β	$E_{\rm pk}$ (keV)	kT (keV)	C-Stat/dof
[0.320, 0.320]	CPL	-1.016 ± 0.293	338.3 ± 229	⋯	406.64/361
[0.320, 0.256]	CPL	-0.955 ± 0.309	331.6 ± 212	⋯	414.34/361
[0.256, 0.320]	PL	-1.749 ± 0.434	⋯	⋯	296.47/362
[0.320, 0.448]	PL	-2.150 ± 0.472	⋯	⋯	341.51/362
[0.512, 1024]	BB	⋯	⋯	13.84 ± 4.67	446.40/362
[1.024, 1.536]	BB	⋯	⋯	11.78 ± 2.41	399.07/362
[1.536, 2.048]	BB	⋯	⋯	9.480 ± 1.61	416.05/362

Notes.
[a] The time interval is given to the GBM trigger.
[b] CPL = Comptonized function. PL = Simple power-law function. BB = Blackbody function.

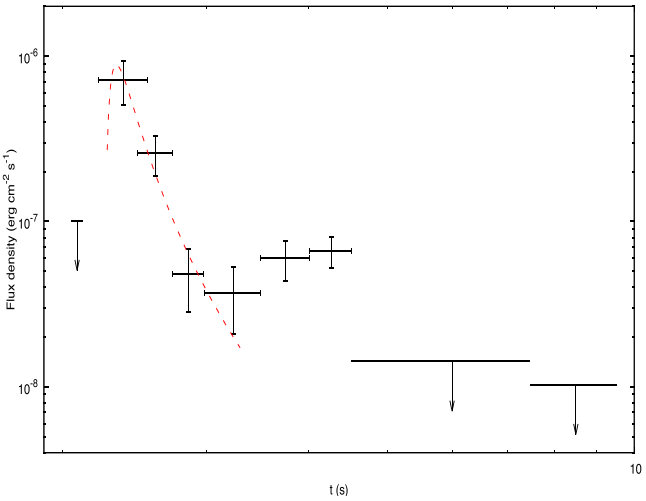

Figure 1. GBM light curve and upper limits in the energy range of 10–1000 keV of GRB 170817A. The red line corresponds to the best-fit curve using a function $F(t) \propto \left(\frac{t-t_0}{t_0}\right)^{-\alpha} e^{-\frac{\tau}{t-t_0}}$ (Vestrand et al. 2006).

column). After the 0.512 s the spectrum fits better using a BB model.

3. Description of the Non-thermal Multiwavelength Observations in GRB 170817A

3.1. Modeling the γ-Ray Flux

3.1.1. Light Curve Analysis and Description

Figure 1 shows the GBM light curve and upper limits in the energy range of 10–1000 keV, although no significant flux was observed above 300 keV. The CPL function showed a cutoff energy of 185 keV and the corresponding isotropic energy obtained was $E_{\gamma,\rm iso} \simeq 5 \times 10^{46}$ erg, with $T_{90} = 2$ s (von Kienlin et al. 2017). The GBM light curve exhibited a peak around ∼1.7 s after the gravitational-wave trigger, followed by a fast decay. The chi-squared (χ^2) minimization method, developed in the ROOT software package (Brun & Rademakers 1997), was used in order to fit the GBM light curve with the function: $F_\nu(t) \propto \left(\frac{t-t_0}{t_0}\right)^{-\alpha_\gamma} e^{-\frac{\tau}{t-t_0}}$ (Vestrand et al. 2006), where t_0 is the starting time, τ is the timescale of the flux rise, and α_γ the power index of fast decay. The best-fit values of parameters are reported in Table 2.

Table 2
Fitted Values of the γ-Ray Data

γ-ray Flux		
Decay slope	α_γ	2.85 ± 0.35 (4.27/4)
Starting time (s)	t_0	2.0 ± 0.1 (4.27/4)
Flux rise timescale (s)	τ	0.4 ± 0.1 (4.27/4)

Note. The chi-squared minimizations (χ^2/n.d.f.) are reported in parentheses.

We derive the spectral parameters of GBM data for different time intervals, as shown in Table 1. Two different time intervals, starting from −0.320 s, were used to fit with a CPL function. The best-fit value of the spectral index for the interval [−0.320 s, 0.256 s] was -0.955 ± 0.309. The remaining time interval was divided in two and analyzed with a PL function. For the interval [0.256 s, 0320 s] a spectral index of -1.749 ± 0.434 was obtained and for interval [0.320 s, 0.448 s] the corresponding spectral index was -2.150 ± 0.472. The spectral fit parameters associated with the γ-ray peak reveal a hard-to-soft spectral evolution.

Veres et al. (2018) analyzed, in the GBM data, the evolution of the peak energy with a CPL model. Using a simple PL $E_{\rm peak} \propto (t - t_{\rm shift})^{-q}$ to model the decay phase, they obtained the best-fit value of $q = 0.97 \pm 0.35$ for $t_{\rm shift} = -0.15 \pm 0.04$ s.

Based on the best-fit values obtained from the analysis of the GBM data and reported in Tables 1 and 2, we discuss the origin of the γ-ray light curve in terms of internal and external shocks.

1. The γ-ray peak $\delta t_{\rm var}/T_{90} \simeq 1$ does not show strong variability that disfavors the internal shock model. The principal motivation for evoking internal shocks is related to the observation of variable γ-ray light curves. In the framework of internal collisions, more than one γ-ray peak is expected, with a variability timescale much shorter than the duration of the main activity $\delta t_{\rm var}/t \ll 1$ (Rees & Meszaros 1994; Kobayashi et al. 1997; Burrows et al. 2005). The properties of several light curves exhibiting one single peak without variability have been explained in the framework of forward/reverse shocks and high-latitude emission (i.e., GRB 970508, GRB 021211, GRB 050406 and others; Kumar & Panaitescu 2003; McMahon et al. 2004, 2006; Nakar & Piran 2004; Kobayashi et al. 2007; Peng et al. 2009; Lu et al. 2010). In the case of the short-lived reverse shock, it can generate a γ-ray, X-ray, or optical peak with $\delta t_{\rm var}/t \simeq 1$ depending on microphysical parameters and the circumburst density (Kobayashi et al. 2007; Fraija et al. 2016a). Therefore, the emission

generated by the reverse shock could in principle describe naturally the variability timescale of the γ-ray light curve.

2. The value of temporal index $\alpha_\gamma = 2.85 \pm 0.35$ observed during the peak decay phase is consistent with the high-latitude afterglow emission. The most adopted interpretation to account for the peak decay phase in the optical, X-ray, and γ-ray bands, is attributed to delayed photons arriving from high latitudes (curvature effect). Kumar & Panaitescu (2000) showed that the evolution of the observed flux, when it is originated at high latitudes, is $F_{\rm obs} \propto t^{\beta-2}$. The values of the spectral index, β, correspond to the low $-\frac{1}{2}\left(\frac{1-p}{2}\right)$ and high-energy $-\frac{p}{2}\left(-\frac{p}{2}\right)$ photon indexes of the synchrotron self-Compton (SSC)/synchrotron spectrum in the fast (slow) cooling regime. Taking into consideration the typical values of the spectral power index for external shocks, $2.2 \leqslant p \leqslant 2.6$ (e.g., see; Kumar & Zhang 2015), the high-latitude afterglow flux is expected to evolve as $F_\nu \propto t^{-\alpha}$ with $2.5 \leqslant \alpha \leqslant 3.2$, which is in accordance with the value obtained of peak decay index $\alpha_\gamma = 2.85 \pm 0.35$. Similar results have been found in a large determined group of GRBs when the peak has been modeled through SSC/synchrotron reverse-shock emission at high latitudes (i.e., see Kobayashi & Zhang 2003; Zhang et al. 2003, 2006; Zhang & Kobayashi 2005; O'Brien et al. 2006; Kobayashi et al. 2007; Fraija et al. 2016b, 2017a, 2017b). On the other hand, based on observations, the typical values of decay index phase associated with internal shocks are $5 \lesssim \alpha \lesssim 7$ (Fan & Wei 2005; Mészáros 2006; Zhang et al. 2006; Kumar & Zhang 2015), which decays faster than that observed in this burst.

3. The evolution of peak energy at hundreds of keVs during the decay phase $q = 0.97 \pm 0.35$ (Veres et al. 2018) is consistent with the SSC energy break of the reverse shock from high latitudes. Several authors have studied the spectral evolution of distinct pulses during γ-ray prompt emission. By analyzing the peak decay phase during the prompt emission, some bursts have provided evidence of the synchrotron emission in the fast-cooling and slow-cooling regime from external shocks (Giblin et al. 1999; Zhang et al. 2003; Panaitescu 2007; Fraija et al. 2017a, 2017b).

When SSC/synchrotron spectral breaks are observed coming from high latitudes/off-axis ($\epsilon^{i,\rm off}$ for syn or SSC), Ioka & Nakamura (2017) proposed that these spectral breaks must be rescaled as $\epsilon^{i,\rm off} \propto \Gamma^{-2}\epsilon^{i,\rm on}$ with Γ the bulk Lorentz factor and $\epsilon^{\rm syn,on}$ the energy break viewed in an on-axis outflow. Following Kobayashi (2000), Fraija et al. (2016b), and Sari et al. (1998), we re-scale the quantities associated with the internal and external shocks.

(i) Internal shocks. Given the bulk Lorentz factor in the coasting phase $\Gamma \propto t^0$ and the magnetic field in the freezing regime $B \propto t^0$, the synchrotron emission evolves as $\epsilon^{\rm syn,off}_{\rm pk} \propto \Gamma^{-2}(\Gamma\,\gamma_e^2\,B) \propto B^{-3}\,\Gamma^{-3}\,t^{-2} \propto t^{-2}$ (Derishev 2007). We consider a "typical" electron Lorentz factor as one that has the average of the electron distribution $\langle\gamma_e\rangle = \frac{U_e}{m_e\,N_e}$ (Piran 1999). These quantities can be calculated using two different ways. 1: the energy density given to accelerate electrons is $U_e = \epsilon_e\,U = \epsilon_e\,\gamma_{\rm sh}\,N_p\,m_p$ and the electron number density can be estimated as $N_e \simeq N_p$ (Piran 1999). In this case, the average electron Lorentz factor becomes $\langle\gamma_e\rangle = \frac{m_p}{m_e}\epsilon_e\gamma_{\rm sh}$. 2: the energy density given to accelerate electrons is $U_e = \frac{m_e\,A_e}{(p-2)}\gamma_{e,\rm mi}^{-p+2}$ and the electron number density can be estimated as $N_e = \frac{m_e\,A_e}{(p-1)}\gamma_{e,\rm mi}^{-p+1}$ for $p > 2$ and $\gamma_{e,\rm mi} \ll \gamma_{e,\rm ma}$. Therefore, in this case $\langle\gamma_e\rangle = \frac{p-1}{p-2}\,\gamma_{e,\rm mi}$. Here, $\gamma_{\rm mi}$ and $\gamma_{\rm ma}$ are the minimum and maximum electron Lorentz factors, respectively, and $\gamma_{\rm sh}$ is the relative Lorentz factor across the internal shock (Piran 1999). Considering both cases and the magnetic field given by $B \simeq \sqrt{\gamma_{\rm sh}}\,\epsilon_B^{1/2}\,\Gamma^{-3}\,L_j^{1/2}\,t_\nu^{-1}$, the electrons accelerated and cooled down in internal shocks via synchrotron radiation reach a peak energy at (e.g., see Fraija et al. 2017a)

$$\epsilon^{\rm syn,on}_{\rm pk} \simeq \begin{cases} 0.4\ {\rm MeV}\ \varepsilon_{e,-0.3}^2\gamma_{\rm sh}^2 \\ 0.6\ {\rm MeV}\ \gamma_{\rm mi,3}^2 \end{cases} \times \left(\frac{1.01}{1+z}\right)\sqrt{\gamma_{\rm sh}}\,\varepsilon_{B,-1}^{1/2}\,\delta t_{\rm var,0}^{-1}\Gamma_3^{-2}L_{j,49}^{1/2}. \quad (1)$$

The microphysical parameters ε_e and ε_B are the fractions of energy given to accelerate electrons and generate/amplify the magnetic field, respectively, and L_j is the jet luminosity. Hereafter, the convention $Q_{\rm x} = Q/10^x$ in c.g.s. units is adopted. Including pair formation, an upper limit for the peak energy can be estimated as Guetta et al. (2001)

$$\epsilon^{\rm syn,on}_{\rm pk} \lesssim 3.3\ {\rm MeV}\left(\frac{1+z}{1.01}\right)^{-1} L_{j,49}^{-1/5}\Gamma_3^{\frac{4}{3}}\,t_{\nu,0}^{\frac{1}{6}}\varepsilon_{B,-1}^{\frac{1}{2}}\,\varepsilon_{e,-0.3}^{\frac{4}{3}}. \quad (2)$$

The peak energy observed from high latitudes/off-axis jet has to be rescaled by $\epsilon^{\rm off}_{\rm pk} \simeq b^{-1}\epsilon^{\rm syn,on}_{\rm pk}$ with $b = 1 + \Gamma^2\Delta\theta^2$ and $\Delta\theta = \theta_{\rm obs} - \theta_j$. In this case, the observed energy $\epsilon^{\rm syn,off}_{\rm pk} \simeq 10\ {\rm eV}\ \Gamma_3^{-2}\Delta\theta_{15^\circ}^{-2}$ indicates that it can hardly reach values as high as hundreds of keVs. Therefore, the standard internal shocks cannot straightforwardly explain the evolution with the time of peak energy at hundreds of keVs.

(ii) Forward shock: given the evolution of the magnetic field $B \propto t^{-3/8}$, the bulk Lorentz factor $\Gamma \propto t^{-3/8}$, the minimum and cooling electron Lorentz factors $\gamma_{m,f} \propto t^{-3/8}$ and $\gamma_{c,f} \propto t^{1/8}$ (Sari et al. 1998), respectively, the synchrotron spectral breaks evolve as $\epsilon^{\rm syn,off}_{m,f} \propto B\,\Gamma^{-3}\,\gamma_{{\rm em},f} \propto t^{-3/4}$ and $\epsilon^{\rm syn,off}_{c,f} \propto B^{-5}\,\Gamma^{-3}\,t^{-2} \propto t^{1/4}$. The SSC spectral breaks evolve as $\epsilon^{\rm ssc,off}_{m,f} \propto \gamma^2_{m,r}\,\epsilon^{\rm syn,off}_{m,f} \propto t^{-3/2}$ and $\epsilon^{\rm ssc,off}_{c,f} \propto \gamma^2_{c,f}\,\epsilon^{\rm syn,off}_{c,f} \propto t^{1/2}$. The subindex "$f$" indicates the forward shock.

The synchrotron spectral break $\epsilon^{\rm syn,off}_{m,f} \propto t^{-3/4}$ is the only spectral break that agrees with the peak energy evolution. The synchrotron spectral break is given by

$$\epsilon^{\rm syn,off}_{m,f} \simeq 0.3\ {\rm keV}\left(\frac{1+z}{1.01}\right)^{\frac{1}{2}} \varepsilon_{e,-0.3}^2\,\varepsilon_{B,f,-1}^{\frac{1}{2}}\,E_{51}^{\frac{1}{2}}\,\Gamma_{2.5}^{-2}\,\Delta\theta_{10^\circ}^{-2} \times t_0^{-\frac{3}{2}},$$

where $E = E_{\gamma,\rm iso}/\eta$ is the isotropic equivalent kinetic energy with η the kinetic efficiency. It shows that although synchrotron spectral break ($\epsilon^{\rm syn,off}_{m,f}$) agrees with the peak energy evolution, it cannot reach the values of energies at hundreds of keVs.

(iii) Reverse shock in the thick- (thin-) shell case: given the evolution of the magnetic field $B \propto t^{-1/4}(t^0)$, the bulk Lorentz factor $\Gamma \propto t^{-1/4}(t^0)$, the minimum and cooling electron Lorentz factors $\gamma_{m,r} \propto t^{1/4}(t^3)$ and $\gamma_{c,r} \propto t^{-1/4}(t^{-1})$ (Kobayashi 2000), respectively, before the crossing time, the synchrotron spectral breaks evolve as $\epsilon^{\rm syn,off}_{m,r} \propto t^{1/2}(t^6)$ and $\epsilon^{\rm syn,off}_{c,r} \propto t^{-1/2}(t^{-2})$. The SSC spectral breaks evolve as $\epsilon^{\rm ssc,off}_{m,r} \propto t\,(t^{12})$ and $\epsilon^{\rm ssc,off}_{c,r} \propto t^{-1}(t^{-4})$. Taking into account that the quantities after the crossing time vary as $B \propto t^{-13/24}(t^{-4/7})$, $\Gamma \propto t^{-7/16}(t^{-2/5})$, $\gamma_{m,r} \propto t^{-13/48}(t^{-2/7})$, and $\gamma_{c,r} \propto t^{25/48}(t^{19/35})$, the synchrotron

spectral breaks evolve as $\epsilon_{m,r}^{\rm syn,off}\propto t^{-0.65}(t^{-0.74})$ and $\epsilon_{m,r}^{\rm syn,off}\propto t^{0.94}(t^{0.91})$. The SSC spectral breaks evolve as $\epsilon_{m,r}^{\rm ssc,off}\propto t^{-1.18}(t^{-1.31})$ and $\epsilon_{c,r}^{\rm ssc,off}\propto t^{1.98}(t^{1.99})$. The subindex "$r$" indicates the reverse shock.

The SSC and synchrotron spectral breaks that agree with the peak energy evolution are $\epsilon_{m,r}^{\rm syn,off}\propto t^{-0.65}(t^{-0.74})$ and $\epsilon_{m,r}^{\rm ssc,off}\propto t^{-1.18}(t^{-1.31})$, respectively. The SSC and synchrotron spectral breaks are given by Kobayashi (2000) and Fraija et al. (2016b)

$$\epsilon_{m,r}^{\rm syn,on}\simeq 16.2\ {\rm eV}\left(\frac{1+z}{1.01}\right)^{-1}\varepsilon_{e,-0.3}^{2}\,\varepsilon_{B,r,-1}^{\frac{1}{2}}\,\Gamma_{2.8}^{2}\,n_0^{\frac{1}{2}},$$

$$\epsilon_{m,r}^{\rm ssc,on}\simeq 13.4\ {\rm MeV}\left(\frac{1+z}{1.01}\right)^{-\frac{7}{4}}\varepsilon_{e,-0.3}^{4}\,\varepsilon_{B,r,-1}^{\frac{1}{2}}\,\Gamma_{2.8}^{4}\,n_0^{\frac{3}{4}}\,E_{51}^{-\frac{1}{4}}\times t_{\rm cr,0}^{\frac{3}{4}},$$

which have to be rescaled again by $(1+\Gamma^2\Delta\theta^2)^{-1}$ (Ioka & Nakamura 2017). The term $t_{\rm cr}$ is the shock crossing time. The parameter n corresponds to the circumburst density. For this analysis, the bulk Lorentz factor corresponds to that one associated with the reverse shock. This value can be estimated by taking into consideration the four-region structure during the shock: (1) the unshocked ISM with density n_1, (2) the shocked ISM, (3) the shocked shell material, and (4) the unshocked shell material with density n_4 and the equations governing the shocks with the jump conditions $\frac{n_4}{n_1}\simeq\frac{(\gamma_3-1)(4\gamma_3+3)}{(\gamma_{34}-1)(4\gamma_{34}+3)}$ and $\gamma_{34}\simeq\frac{1}{2}\left(\frac{\gamma_4}{\gamma_3}+\frac{\gamma_3}{\gamma_4}\right)$ (Blandford & McKee 1976; Sari & Piran 1995), with γ_{34} being the relative Lorentz factor between the upstream and downstream regions, $\gamma_3\equiv\Gamma_r$ and $\gamma_4\equiv\Gamma$ are the reverse and initial Lorentz factors, respectively (Kobayashi 2000). For the relativistic case, i.e., $\gamma_{34}\gg 1$, the bulk Lorentz factor of the reverse shock is

$$\Gamma_r\simeq\sqrt{\frac{\Gamma}{2}}\left(\frac{n_4}{n_1}\right)^{1/4}. \quad (3)$$

For typical values of the initial bulk Lorentz factor $300\leqslant\Gamma\leqslant 600$ and densities of unshocked ISM and shell $n_4\simeq n_1$, the bulk Lorentz factor becomes $12.3\leqslant\Gamma_r\leqslant 17.3$. For the case of $\Gamma_r=15$, SSC and synchrotron spectral breaks have to be rescaled by $\approx 7\times 10^{-2}\Gamma_{r,1.2}^{-2}\,\Delta\theta_{15^\circ}^{-2}$. Therefore, the characteristic break of SSC reverse-shock emission agrees with the evolution of peak energy at hundreds of keVs during the decay phase.

4. The hard-to-soft spectral-index evolution (from -1.749 ± 0.434 to -2.150 ± 0.472) seems to be consistent with the SSC/synchrotron spectrum that originated in external shocks. Ultra-relativistic electrons confined in a magnetic field are cooled down by synchrotron and SSC radiation. The high and low spectral indexes in the fast(slow)-cooling regime are $-\frac{1}{2}\left(-\frac{p-1}{2}\right)$ and $-\frac{p}{2}\left(-\frac{p}{2}\right)$, respectively. Given the typical values of the spectral power index for external shocks, $2.2\leqslant p\leqslant 2.6$ (e.g., see; Kumar & Zhang 2015), the SSC/synchrotron spectrum $\nu F_\nu\propto\nu^{-(\beta+1)}$ with $1.5(1.6)\leqslant\beta+1\leqslant 2.3(2.3)$ agrees with the spectral-index evolution for fast (slow)-cooling regime.

The previous analysis, performed on the temporal and spectral features of the γ-ray light curve (see Figure 1 and Tables 1 and 2), illustrates that: (i) the characteristic break of SSC reverse shock agrees with the evolution of peak energy at hundreds of keVs during the decay phase, while synchrotron emission from internal and forward shocks cannot explain this evolution.; (ii) the reverse-shock emission can reproduce, in a more natural way, the observed variability timescale than internal shock emission; and (iii) the temporal and spectral indexes of synchrotron/SSC emission, originating from external shocks, are consistent with the spectral-index evolution and the high-latitude afterglow model. Therefore, we argue that the SSC reverse-shock emission in the fast-cooling regime reproduce the temporal and spectral features of the γ-ray light curve. In the following subsection the SSC spectrum in the fast-cooling regime is used to describe the the γ-ray flux.

3.1.2. Theoretical Model

The SSC spectral breaks and fluxes are determined by the spectral break evolution between forward and reverse shocks (Zhang & Kobayashi 2005; Fraija 2015; Fraija et al. 2016a). The SSC spectrum in the fast-cooling regime is given by Ioka & Nakamura (2017)

$$F_{\nu,r}^{\rm ssc,on}=F_{\rm max,r}^{\rm ssc,on}\left(\frac{\epsilon_\gamma}{\epsilon_{c,r}^{\rm ssc,on}}\right)^{-\frac{1}{2}}\ \text{for}\ \epsilon_{c,r}^{\rm ssc,on}<\epsilon_\gamma<\epsilon_{m,r}^{\rm ssc,on}, \quad (4)$$

and once the characteristic break energy passes through the γ-ray band $\epsilon_\gamma\approx 100$ keV at $\sim t_{\rm cr}\,\epsilon_{m,r}^{\rm ssc,on}/\epsilon_\gamma$, the SSC flux begins evolving in the following power-law segment of the light curve $F_{\rm max,r}^{\rm ssc,on}\left(\frac{\epsilon_{m,r}^{\rm ssc,on}}{\epsilon_{c,r}^{\rm ssc,on}}\right)^{-\frac{1}{2}}\left(\frac{\epsilon_\gamma}{\epsilon_{m,r}^{\rm ssc,on}}\right)^{-\frac{p}{2}}$ for $\epsilon_{c,r}^{\rm syn,on}<\epsilon_{m,r}^{\rm syn,on}<\epsilon_\gamma$. The SSC energy breaks and the maximum fluxes when reverse shock evolves in the thick shell are given explicitly in Fraija et al. (2012). These quantities viewed off-axis must be corrected by

$$\epsilon_{m/c,r}^{\rm ssc,off}=b^{-1}\epsilon_{m/c,r}^{\rm ssc,on},\ \text{and}\ F_{\rm max,r}^{\rm ssc,off}=b^{-3}F_{\rm max,r}^{\rm ssc,on}. \quad (5)$$

To find the best-fit values that reproduce the data with our off-axis model, we perform the Bayesian statistical method of Markov-Chain Monte Carlo (MCMC) simulations. Our model is fully described by a set of seven parameters, $\Xi_{\rm rev}=\{n,\tilde{E},\Delta\theta,p,\Gamma_r,\varepsilon_{B,r},\varepsilon_e\}$, with an extra parameter of σ for the likelihood of the MCMC. We generate samples of the posterior for our off-axis model using the No-U-Turn Sampler (NUTS) from the PyMC3 python distribution (Salvatier et al. 2016). In order to fit data, we run the model for fluxes with a total of 14,000 samples and 3000 tuning steps, which are to be discarded after tuning. The priors are assigned independently, with a mixture of different continuous probability distributions functions and standard deviations. The parameters p, Γ_r, and n are given normal distributions, $\Delta\theta$ a uniform distribution and $\varepsilon_{B,r}$, ε_e, and $\tilde{E}$ are given modified normal distributions. Output is given by means of a corner plot (Foreman-Mackey 2016) on which the diagonal is a one-dimensional kernel plot of the posterior probability distribution function and the off-diagonal are the bidimensional kernel plots. Hereafter, the values of cosmological parameters $H_0=71\ {\rm km\,s^{-1}\,Mpc^{-1}}$, $\Omega_m=0.27$, $\Omega_\lambda=0.73$ are adopted (Spergel et al. 2003).

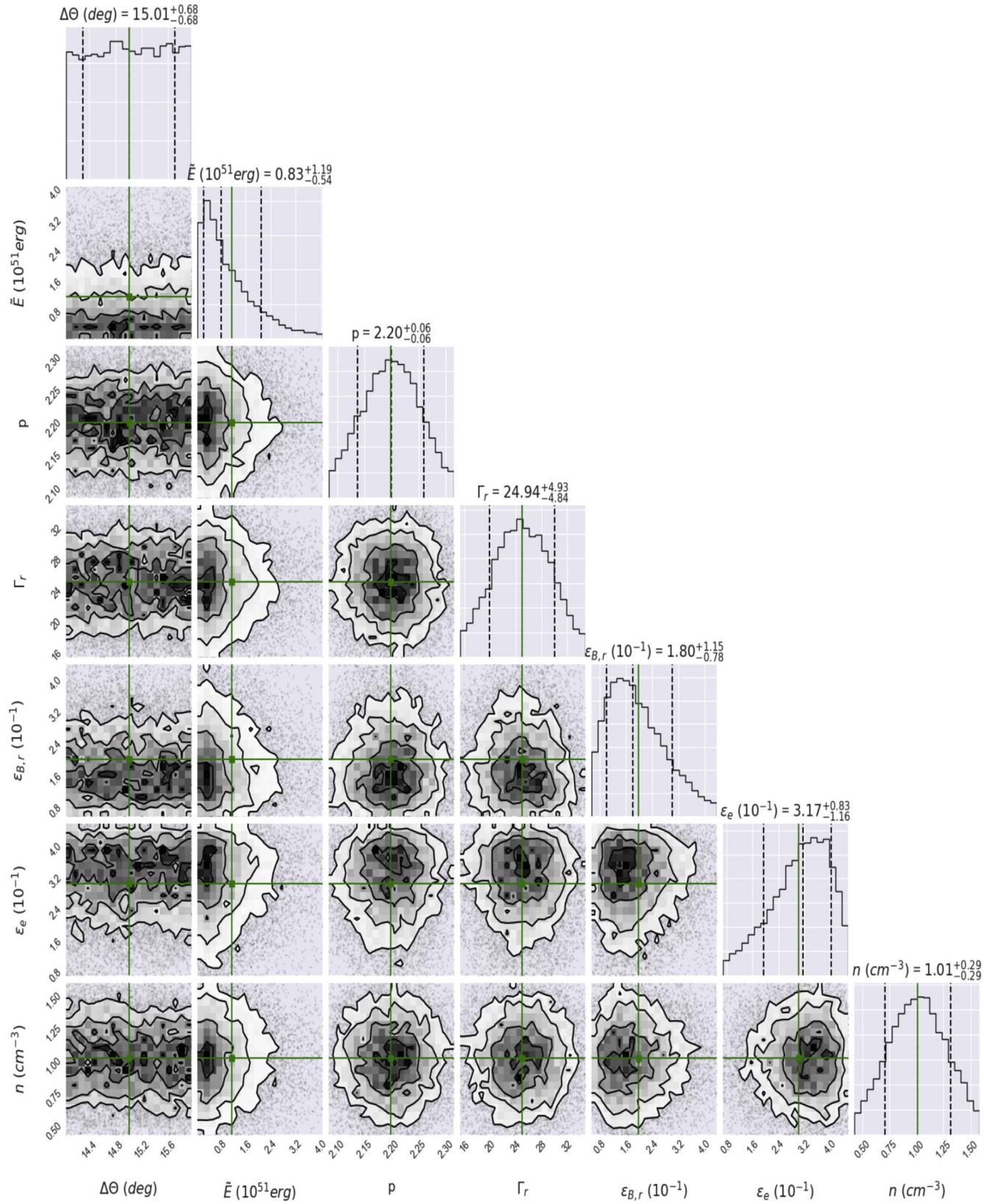

Figure 2. Corner plot comparing the results obtained from the MCMC simulation for each parameter. Fit result for GBM γ-ray data using a SSC reverse-shock model in homogeneous density as described in Section 2.1. The labels above the 1D kernel plots indicate the median, and 0.15 and 0.85 quantiles of each parameter. The best-fit value is shown in green.

Table 3
The Median and Symmetrical Quantiles (0.15, 0.5, 0.85) after Describing the γ-Ray GBM Peak with Our Model

Parameters	Median
$\tilde{E}$ (10^{51} erg)	$0.83^{+1.19}_{-0.54}$
n (cm^{-3})	$1.01^{+0.29}_{-0.29}$
Γ_r	$24.94^{+4.93}_{-4.84}$
p	$2.20^{+0.06}_{-0.06}$
$\Delta\theta$ (deg)	$15.01^{+0.68}_{-0.68}$
ε_e (10^{-1})	$3.17^{+0.83}_{-1.16}$
$\varepsilon_{B,r}$ (10^{-1})	$1.80^{+1.15}_{-0.78}$

Figure 2 shows the corner plots obtained from the MCMC simulation for each parameter using the SSC reverse-shock model. The best-fit values in this figure are shown in green. The median of the posterior distributions, alongside the symmetrical 35% quantiles, are reported in Table 3.

3.2. Modeling the Non-thermal X-Ray, Optical, and Radio Data

3.2.1. Light Curve Analysis and Description

Several X-ray observations were carried out during the eight days following the merger, and provide constraining limits (i.e., see Margutti et al. 2017a). On the ninth day, the *Chandra* X-ray observatory reported a faint X-ray flux from the direction of the binary NS merger (Troja et al. 2017b). From the 108th to 256th days post-GW trigger, *Chandra* and *XMM-Newton* reported detections (Margutti et al. 2017b; Haggard et al. 2018). The *Hubble Space Telescope* (*HST*) observed optical non-thermal fluxes with magnitudes 26.44 ± 0.14 mag (Lyman et al. 2018) and 26.90 ± 0.25 mag (Margutti et al. 2018) at ∼110 and 137 days, respectively, after the merger. On 2018 March 23, *HST* provides an upper limit of >0.070 μJy (Alexander et al. 2018). Since the sixteenth day post-trigger and for more than seven months, VLA has reported a faint radio flux at 3 and 6 GHz (Alexander et al. 2017; Hallinan et al. 2017; Mooley et al. 2017; Troja et al. 2017a).

In order to describe, first, the X-ray, optical, and radio light curves during the increasing phase, we consider these light curves up to 145 ± 20 days and the broadband SED in three separate periods: at 15 ± 2, 110 ± 5, and 145 ± 20 days. The X-ray and radio (6 and 3 GHz) light curves up to 145 ± 20 days were adjusted to simple power laws $F_\nu \propto t^{-\alpha_i}$ (for $i = X$, 6 GHz and 3GHz), and the broadband SED at 15 ± 2, 110 ± 5 and 145 ± 20 days were fitted with $F_\nu \propto \nu^{-\beta_i}$. The best-fit values of temporal and spectral indexes obtained with the χ^2 test implemented in the ROOT software package are reported in Table 4. Given the best-fit values obtained up to 145 ± 20 days, the multiwavelength fluxes can be described as $\propto t^{0.76\pm0.18}\ \nu^{-0.58\pm0.15}$ for the X-ray, optical, and radio data.

Afterglow emission is generated when the relativistic jet encounters the homogeneous medium and sweeps up enough circumburst material. The synchrotron forward-shock model is the most favorable one to describe the late-time multi-wavelength observations. Taking into account the closure relations of the standard synchrotron forward-shock model, the X-ray, optical, and radio (6 and 3 GHz) fluxes are evolving in the slow-cooling regime corresponding to the power-law segment (Sari et al. 1998):

$$F^{\rm syn,on}_{\nu,f} = F^{\rm syn,on}_{{\rm max},f}\left(\frac{\epsilon_\gamma}{\epsilon^{\rm syn,on}_{m,r}}\right)^{-\frac{p-1}{2}} \quad \text{for } \epsilon^{\rm syn}_{m,r} < \epsilon_\gamma < \epsilon^{\rm syn,on}_{c,r}, \tag{6}$$

with $p = 2\beta + 1 \approx 2.2$ and

$$\epsilon^{\rm syn,on}_{m,f} \propto t^0\,\Gamma^4,\ \epsilon^{\rm syn,on}_{c,f} \propto t^{-2}\,\Gamma^{-4} \quad \text{and}$$
$$F^{\rm syn,on}_{{\rm max},f} \propto E\,t^0\Gamma^0. \tag{7}$$

Considering the evolution of the bulk Lorentz factor, $\Gamma \propto t^{-\frac{3}{8}}$, the flux varies as $F^{\rm syn,on}_{\nu,f} \propto t^{-\frac{3(p-1)}{4}}$. Given the observed temporal index reported in Table 4, the value of the electron distribution would be $p \approx -0.07$, which is inconsistent with the value obtained from the broadband SED ($p \approx 2.2$). While the evolution of the synchrotron flux as a function of the energy is well-described, the evolution of it with time fails. This inconsistency is due to the evolution of the bulk Lorentz factor.

Given that the standard synchrotron afterglow model cannot account for the X-ray, optical and radio light curves of GRB 170817A, we consider the synchrotron forward-shock model to be off-axis when the matter in the outflow is parameterized through a power law velocity distribution.

3.2.2. Theoretical Model

We consider that the jet concentrated within an opening angle θ_j "top-hat jet" producing the afterglow emission is not aligned with the observer's line of sight and the ejecta has an equivalent kinetic energy parameterized by a power-law distribution as $\tilde{E}\,(\beta\Gamma)^{-\alpha_s}$ where $\tilde{E}$ is the fiducial energy, $\alpha_s = 1.1$ for $\beta\Gamma \gg 1$ and $\alpha_s = 5.2$ for $\beta\Gamma \ll 1$ for the adiabatic case (Sari & Mészáros 2000; Tan et al. 2001; Hotokezaka et al. 2013; Kyutoku et al. 2014; Barniol et al. 2015; Hotokezaka & Piran 2015; Fraija et al. 2018). Taking into account the relativistic regime ($\beta\Gamma \gg 1$), we propose that the corresponding equivalent kinetic energy for $\theta_{\rm obs} \gtrsim 2\theta_j$ is given by

$$E_k = b^{-3}\,\tilde{E}\,\Gamma^{-\alpha_s}$$
$$\simeq \Delta\theta^{-6}\Gamma^{-\delta}\tilde{E}, \tag{8}$$

for $\Gamma^2\Delta\theta^2 \gg 1$ with $\Delta\theta = \theta_{\rm obs} - \theta_j$ and $\delta = \alpha_s + 6$.

Considering the adiabatic evolution of the forward shock (Blandford & McKee 1976; Sari 1997), the fiducial energy is given by $\tilde{E} = 16/17\pi\Delta\theta^6\Gamma^{\delta+2}R^3 n\,m_p$ (Blandford & McKee 1976; Sari 1997) with m_p being the proton mass and R being the deceleration radius. In this case, the bulk Lorentz factor evolves as

$$\Gamma = 7.8\left(\frac{1+z}{1.01}\right)^{\frac{3}{\delta+8}} n_{-4}^{-\frac{1}{\delta+8}}\,\tilde{E}_{51}^{\frac{1}{\delta+8}}\,\Delta\theta_{20^\circ}^{-\frac{6}{\delta+8}}\,t_{1\,\rm d}^{-\frac{3}{\delta+8}}. \tag{9}$$

Table 4
Fitted Values of the X-Ray, Optical, and Radio Data

Light Curve		
X-ray flux		
Rising slope	$\alpha_{\rm X}$	0.76 ± 0.18 (0.45/4)
Optical flux		
Rising slope	$\alpha_{\rm opt}$	...
Radio flux		
3 GHz		
Rising slope	$\alpha_{\rm 3GHz}$	0.85 ± 0.12 (1.67/3)
6 GHz		
Rising slope	$\alpha_{\rm 6GHz}$	0.75 ± 0.19 (11.16/6)
Spectral Energy Distribution		
Spectral slope (16 ± 2 days)	$\beta_{\rm 16d}$	-0.59 ± 0.11 (3.796/7)
Spectral slope (110 ± 5 days)	$\beta_{\rm 110d}$	-0.58 ± 0.15 (19.19/20)
Spectral slope (145 ± 20 days)	$\beta_{\rm 145d}$	-0.59 ± 0.15 (19.19/20)

Note. The chi-squared minimizations (χ^2/n.d.f.) are reported in parentheses.

Replacing Equations (9) and (8) in (7), the synchrotron spectral breaks and the maximum fluxes are

$$\epsilon^{\rm syn}_{m,f} \simeq 7.7 \times 10^{-4}\,{\rm GHz}\left(\frac{1+z}{1.01}\right)^{\frac{4-\delta}{\delta+8}} \varepsilon^{2}_{e,-1}\,\varepsilon^{\frac{1}{2}}_{B,-4}\,n^{\frac{\delta}{2(\delta+8)}}_{-4} \times \tilde{E}^{\frac{4}{\delta+8}}_{51}\,\Delta\theta^{-\frac{24}{\delta+8}}_{20^\circ}\,t^{-\frac{12}{\delta+8}}_{100\,\rm d}$$

$$\epsilon^{\rm syn}_{c,f} \simeq 5.2\,{\rm keV}\left(\frac{1+z}{1.01}\right)^{\frac{\delta-4}{\delta+8}}(1+x)^{-2}\,\varepsilon^{-\frac{3}{2}}_{B,-4}\,n^{-\frac{16+3\delta}{2(\delta+8)}}_{-4} \times \tilde{E}^{-\frac{4}{\delta+8}}_{51}\,\Delta\theta^{\frac{24}{\delta+8}}_{20^\circ}\,t^{-\frac{2\delta+4}{\delta+8}}_{100\,\rm d}$$

$$F^{\rm syn}_{{\rm max},f} \simeq 1.4\,{\rm mJy}\left(\frac{1+z}{1.01}\right)^{\frac{8-2\delta}{\delta+8}} \varepsilon^{\frac{1}{2}}_{B,-4}\,n^{\frac{3\delta+8}{2(\delta+8)}}_{-4}\,D^{-2}_{26.1}\,\tilde{E}^{\frac{8}{\delta+8}}_{51} \times \Delta\theta^{-\frac{48}{\delta+8}}_{20^\circ}\,t^{\frac{3\delta}{\delta+8}}_{100\,\rm d}. \quad (10)$$

Given the new evolution of the synchrotron emission, from Equations (13) and (6), the power-law segment of the synchrotron spectrum in the slow-cooling regime becomes

$$F_{\nu,{\rm inc}} \simeq F_{\nu,{\rm i}}\,t^{\frac{3\delta-6(p-1)}{\delta+8}}_{100\,\rm d}\,\epsilon_\gamma^{-\frac{p-1}{2}}\,A_{\nu,{\rm inc}}, \quad (11)$$

where

$$A_{\nu,{\rm inc}} = \left(\frac{1+z}{1.01}\right)^{-\frac{7\delta+12+p\delta+4p}{2(\delta+8)}} \varepsilon^{p-1}_{e,-1}\,\varepsilon^{\frac{p+1}{4}}_{B,-4}\,n^{\frac{16+\delta(p+5)}{4(\delta+8)}}_{-4}\,D^{-2}_{26.1} \times \tilde{E}^{\frac{6+2p}{\delta+8}}_{51}\,\Delta\theta^{-\frac{12(p+3)}{\delta+8}}_{20^\circ}, \quad (12)$$

and $F_{\nu,i} = \{9.8\times10^{-3},\ 6.5\times10^{-3},\ 1.1\times10^{-5},\ 1.8\times10^{-7}\}$ mJy for $\epsilon_\gamma = \{3\ {\rm GHz}, 6\ {\rm GHz}, 1\ {\rm eV}, 1\ {\rm keV}\}$, respectively. For this case, the flux varies as $F_\nu \propto t^{\frac{3\delta-6(p-1)}{\delta+8}}\,\nu^{-\frac{p-1}{2}}$, which for $\alpha_s \approx 1.1$ and $p \approx 2.2$ it evolves as found after fitting the SED at 15 ± 2, 110 ± 5, and 145 ± 20 days and reported in Table 4. It is worth noting that for $\delta = 0$, the flux $F_{\nu,{\rm dec}} \propto t^{-\frac{3(p-1)}{4}}$ derived in Sari et al. (1998) is recovered.

Since the radiation beaming cone broadens increasingly, it reaches our line of sight later ($\Gamma \sim \Delta\theta^{-1}$; Rees 1999; Sari et al. 1999; Dermer et al. 2000; Granot et al. 2002, 2017). Once the flux reaches our field of view the synchrotron spectral breaks and the maximum flux become

$$\epsilon^{\rm syn}_{m,f} \simeq 2.9 \times 10^{-4}\,{\rm GHz}\left(\frac{1+z}{1.01}\right)^{\frac{6-\alpha_s}{\alpha_s+6}} \times \varepsilon^{2}_{e,-1}\,\varepsilon^{\frac{1}{2}}_{B,-4}\,n^{\frac{\alpha_s-2}{2(\alpha_s+6)}}_{-4}\,\tilde{E}^{\frac{4}{\alpha_s+6}}_{51}\,t^{-\frac{12}{\alpha_s+6}}_{200\,\rm d}$$

$$\epsilon^{\rm syn}_{c,f} \simeq 3.4\,{\rm keV}\left(\frac{1+z}{1.01}\right)^{\frac{\alpha_s-6}{\alpha_s+6}}(1+x)^{-2}\,\varepsilon^{-\frac{3}{2}}_{B,-4}\,n^{-\frac{3\alpha_s+10}{2(\alpha_s+6)}}_{-4} \times \tilde{E}^{-\frac{4}{\alpha_s+6}}_{51}\,t^{-\frac{2\alpha_s}{\alpha_s+6}}_{200\,\rm d}$$

$$F^{\rm syn}_{{\rm max},f} \simeq 1.1\,{\rm mJy}\left(\frac{1+z}{1.01}\right)^{-\frac{4\alpha_s}{\alpha_s+6}} \varepsilon^{\frac{1}{2}}_{B,-4}\,n^{\frac{3\alpha_s+2}{2(\alpha_s+6)}}_{-4} \times D^{-2}_{26.1}\,\tilde{E}^{\frac{8}{\alpha_s+6}}_{51}\,t^{-\frac{3(2-\alpha_s)}{\alpha_s+6}}_{200\,\rm d}. \quad (13)$$

Since $\epsilon^{\rm syn}_{m,f} \leqslant \epsilon_\gamma \leqslant \epsilon^{\rm syn}_{c,f}$, the flux lies in the same power-law segment. It begins decreasing as

$$F_{\nu,{\rm dec}} \simeq F_{{\rm nu},j}\,t^{-\frac{3(\alpha_s-2p)}{\alpha_s+6}}_{200\,\rm d}\,\epsilon_\gamma^{-\frac{p-1}{2}}\,A_{\nu,{\rm dec}}, \quad (14)$$

where

$$A_{\nu,{\rm dec}} = \left(\frac{1+z}{1.01}\right)^{\frac{6p-7\alpha_s-p\alpha_s-6}{2(\delta+8)}} \varepsilon^{p-1}_{e,-1}\,\varepsilon^{\frac{p+1}{4}}_{B,-4}\,n^{\frac{5\alpha_s+6+\alpha_s p-2p}{4(\alpha_s+6)}}_{-4}\,D^{-2}_{26.1} \times \tilde{E}^{\frac{2(p+3)}{\alpha_s+6}}_{51} \quad (15)$$

and $F_{{\rm nu},j} = \{6.1\times10^{-3},\ 4.0\times10^{-3},\ 6.9\times10^{-6},\ 1.1\times10^{-7}\}$ mJy for $\epsilon_\gamma = \{3\ {\rm GHz}, 6\ {\rm GHz}, 1\ {\rm eV}, 1\ {\rm keV}\}$, respectively.

Table 5
The Median and Symmetrical Quantiles (0.15, 0.5, 0.85), Truncated at the Second Decimal, after Describing the X-Rays and Radio Wavelengths at 3 and 6 GHz with Our Model

Parameters	Median		
	Radio (3 GHz)	Radio (6 GHz)	X-ray (1 keV)
$\tilde{E}$ (10^{51} erg)	$0.700^{+0.010}_{-0.010}$	$0.700^{+0.010}_{-0.010}$	$0.701^{+0.010}_{-0.010}$
n (10^{-4} cm^{-3})	$1.010^{+0.010}_{-0.010}$	$1.020^{+0.010}_{-0.010}$	$1.008^{+0.010}_{-0.010}$
p	$2.210^{+0.010}_{-0.010}$	$2.210^{+0.010}_{-0.010}$	$2.230^{+0.010}_{-0.010}$
$\Delta\theta$ (deg)	$15.001^{+0.133}_{-0.136}$	$15.001^{+0.137}_{-0.137}$	$15.001^{+0.133}_{-0.136}$
ε_e (10^{-1})	$2.500^{+0.010}_{-0.010}$	$2.500^{+0.010}_{-0.010}$	$2.498^{+0.010}_{-0.010}$
$\varepsilon_{B,f}$ (10^{-4})	$1.010^{+0.010}_{-0.010}$	$1.100^{+0.010}_{-0.010}$	$0.997^{+0.010}_{-0.010}$
k	$3.000^{+0.010}_{-0.010}$	$3.000^{+0.010}_{-0.010}$	$2.998^{+0.010}_{-0.010}$
α_s	$1.105^{+0.010}_{-0.010}$	$1.095^{+0.010}_{-0.010}$	$1.115^{+0.004}_{-0.007}$

It is worth noting that for $\alpha_s = 0$, the flux $F_{\nu,\rm dec} \propto t^{-p}$ derived in Sari et al. (1999) is recovered.

Therefore, the flux to be used to model the X-ray, optical, and radio data can be summarized as

$$F_\nu = \begin{cases} F_{\nu,\rm inc}, & \text{if} \quad t < t_{\rm peak}, \\ F_{\nu,\rm dec}, & \text{if} \quad t > t_{\rm peak}, \end{cases} \tag{16}$$

where

$$t_{\rm peak} \simeq 86.6 \text{ days } k \left(\frac{1+z}{0.01}\right) n_0^{-1/3} E_{51}^{1/3} \Delta\theta_{20^\circ}^{\frac{\alpha_s+6}{3}}, \tag{17}$$

where the parameter k differs from one model to another, and is introduced to correlate the times of peak flux and the jet break through the viewing and the opening angles (Granot et al. 2002; Nakar et al. 2002).

To find these values, we again perform the Bayesian statistical method of Markov-Chain Monte Carlo (MCMC) simulations. In this case, our model is fully described by a set of eight parameters, $\Xi_{\rm fow} = \{\rm n, \tilde{E}, k, \Delta\theta, p, \alpha_s, \varepsilon_{B,f}, \varepsilon_e\}$, with an extra parameter of σ for the likelihood of the MCMC. For this MCMC run, we utilized 14,000 steps with 7000 tuning steps, which were discarded after tuning. The parameters $\Delta\theta$ and p are given uniform distributions, while the remaining parameters n, $\epsilon_{B,f}$, ϵ_e, k, α_s, and $\tilde{E}$ are given normal distributions. Output is again given by means of a corner plot (Foreman-Mackey 2016) on which the diagonal is a one-dimensional projection of the posterior probability distribution function and the off-diagonal plots are the bidimensional projections.

Figures 3–5 show the corner plots for radio wavelengths (3 and 6 GHz) and X-rays, respectively, obtained from the MCMC simulation for each parameter using our model (Equations (16)). The best-fit values in these figures are shown in green. The median of the posterior distributions, alongside the symmetrical 35% quantiles, are reported in Table 5.

Figure 6 shows the light curves (left) and the spectral energy distributions (right) of the X-ray, optical and radio bands of GRB 170817A.

3.3. Analysis and Implications

3.3.1. The Magnetic Microphysical Parameters

Sari & Piran (1995) derived the hydrodynamic timescales of the reverse shock for a non-magnetized GRB jet. They found that in the absence of magnetization, the crossing time becomes $t_{\rm cr} \simeq \frac{T_{90}}{2}$. The hydrodynamic timescales of the reverse shock powered by a magnetized outflow were investigated by Fan et al. (2004), Zhang & Kobayashi (2005), and Mimica et al. (2009, 2010). Authors reported that general characteristics in the reverse shock vary according to the degree of magnetization in the jet. For instance, when the jet was moderately magnetized with a magnetization parameter in the range of $0.1 \lesssim \sigma \lesssim 1$, then the magnetic microphysical parameter would vary between $0.1 \lesssim \varepsilon_{B,r} \lesssim 0.2$ and the width of the peak generated by the reverse shock became narrower and more prominent, between $\frac{T_{90}}{2} \lesssim t_{\rm cr} \lesssim \frac{T_{90}}{5}$. This result agrees with the value of the magnetic microphysical parameter found after describing the GBM data and the duration of the bright peak ($\sim$0.4 s) observed in the GBM light curve. If the relativistic jet had high magnetization ($\sigma \gg 1$) when it crossed the reverse shock, relativistic particles would be poorly accelerated and the emission drastically decreased (Zhang & Kobayashi 2005; Sironi & Spitkovsky 2011). Therefore, a moderate magnetization ($\sigma \lesssim 1$) is required in order to interpret the GBM bright peak in the reverse-shock framework (Kumar & Panaitescu 2003; Zhang et al. 2003; Fan et al. 2004).

The values of the magnetic microphysical parameters (see Tables 3 and 5) indicate that the magnetic field ratio in the forward-shock and reverse-shock region is $\sim$40. Similarly, the values found also illustrate that synchrotron flux is $\sim 2.5 \times 10^3$ times stronger in the reverse than the forward shock, so there are many more photons available to be scattered via inverse Compton in the reverse shock. This suggests that the outflow carried a significant magnetic field, as reported in sGRB 090510 (Fraija et al. 2016b).

Taking into consideration the typical initial value of the fireball radius ($r_i \sim 10^{6.5}$ cm; Lee et al. 2004, 2005; Nakar 2007), the kinetic equivalent energy and the magnetic microphysical parameter (see Table 3), the magnetic field at the base of the jet is roughly estimated as $B \approx \sqrt{8\varepsilon_{B,i}E_{\gamma,\rm iso}/r_i^3} \approx 10^{15}$ G. The strength of the magnetic field is 3-4 orders of magnitude higher than the usual strength in a NS $\sim 10^{12}$ G. Here, $\varepsilon_{B,i} \approx \varepsilon_{B,r}$ is the initial fraction of total energy given to magnetic field. It shows that GRB 170817A demands more magnetic fields at the base of the jet, thus indicating that the progenitor is entrained with strong magnetic fields.

Just et al. (2016) laid out relativistic and axisymmetric hydrodynamic simulations of a black hole-torus system as remnants of a binary NS merger. They showed that thermal energy via annihilation of neutrinos and antineutrinos abundantly emitted by the hot accretion disk is not long and strong enough for the outflows to break out from the neutrino wind, thus concluding that the neutrino annihilation alone could not power sGRBs from binary NS mergers. Therefore, the energy requirements favor magnetic fields as the responsible mechanism so that the outflow breaks out. Some authors have presented simulations based on general relativistic magnetohydrodynamics to follow the evolution of the magnetic fields in the binary NS merger (Price & Rosswog 2006; Zrake & MacFadyen 2013; Ciolfi et al. 2017). All models proposed show an amplification of magnetic field of up to three orders of magnitude or more. The rapid growth of this field is attributed to the Kevin–Helmholtz instabilities and turbulent and/or differential rotation. Therefore, the most natural process associated with the magnetization of outflow is the magnetic field amplification during the binary NS merger, which is entrained by outflow.

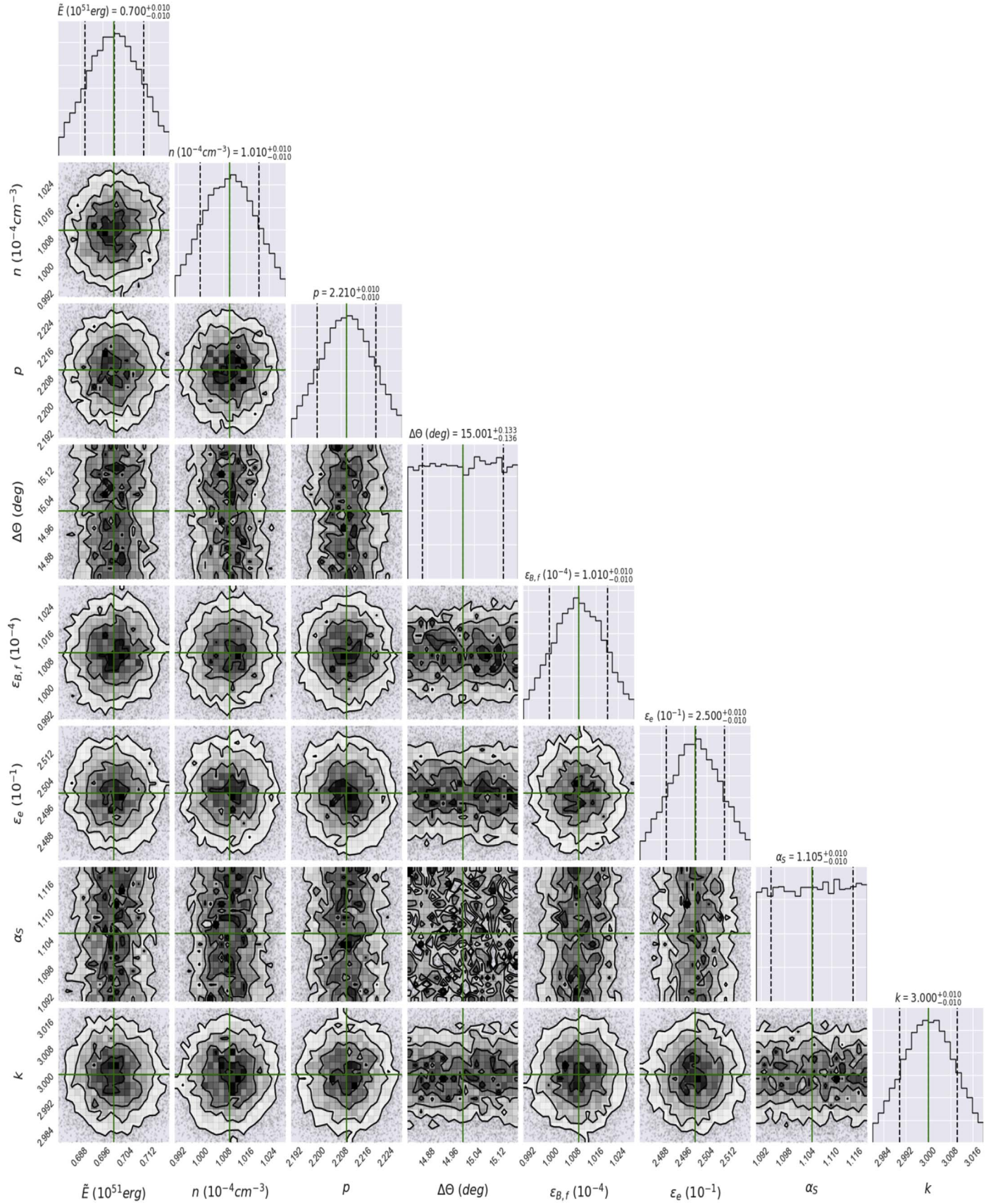

Figure 3. Same as Figure 2, but using a synchrotron forward-shock model to fit the radio (3 GHz) data when the jet producing the afterglow emission is not aligned with the observer's line of sight and the matter in the outflow is parameterized through a power-law velocity distribution (model described in Section 2.2).

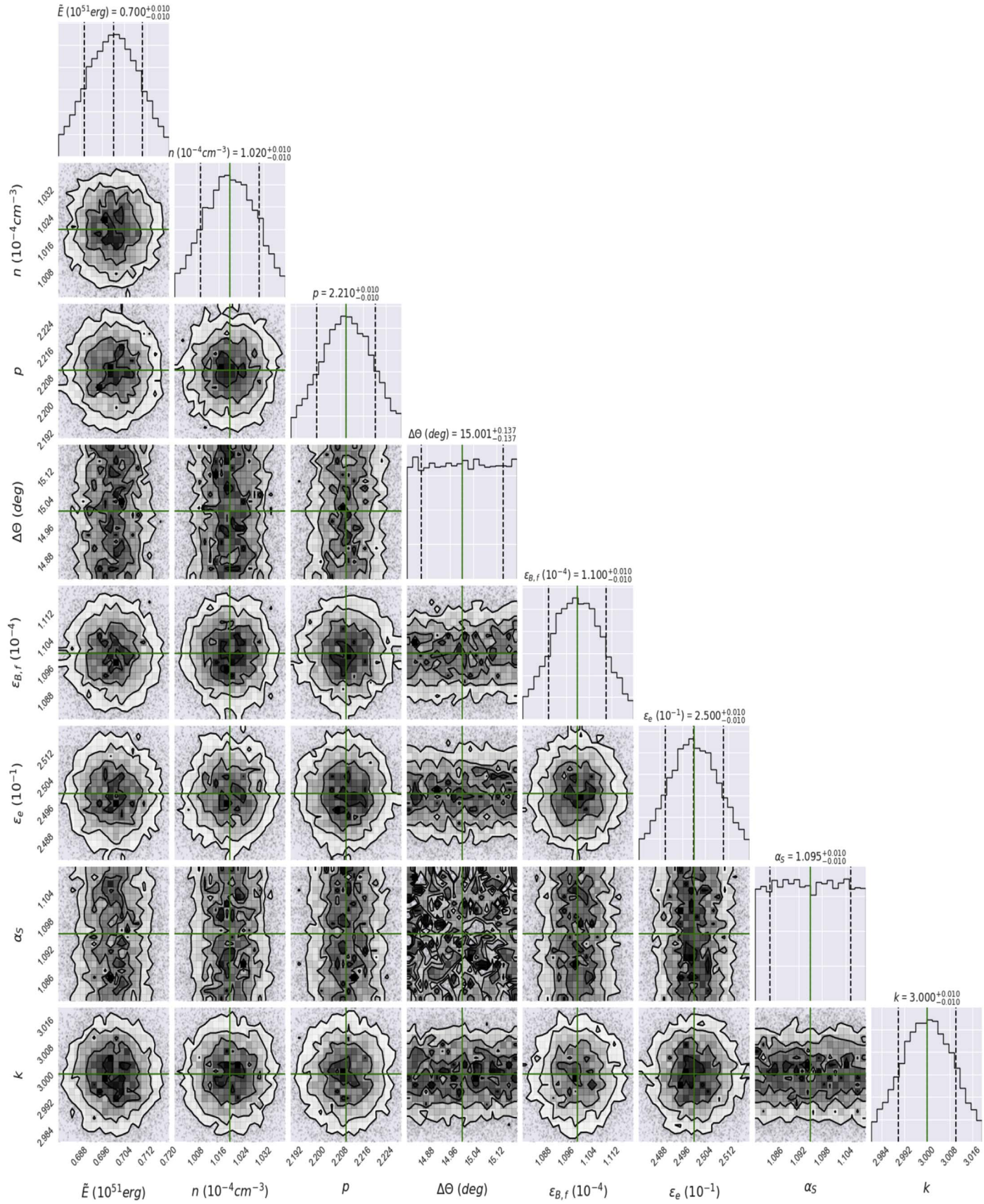

Figure 4. Same as Figure 2, but using a synchrotron forward-shock model to fit the radio (6 GHz) data when the jet producing the afterglow emission is not aligned with the observer's line of sight and the matter in the outflow is parameterized through a power-law velocity distribution (model described in Section 2.2).

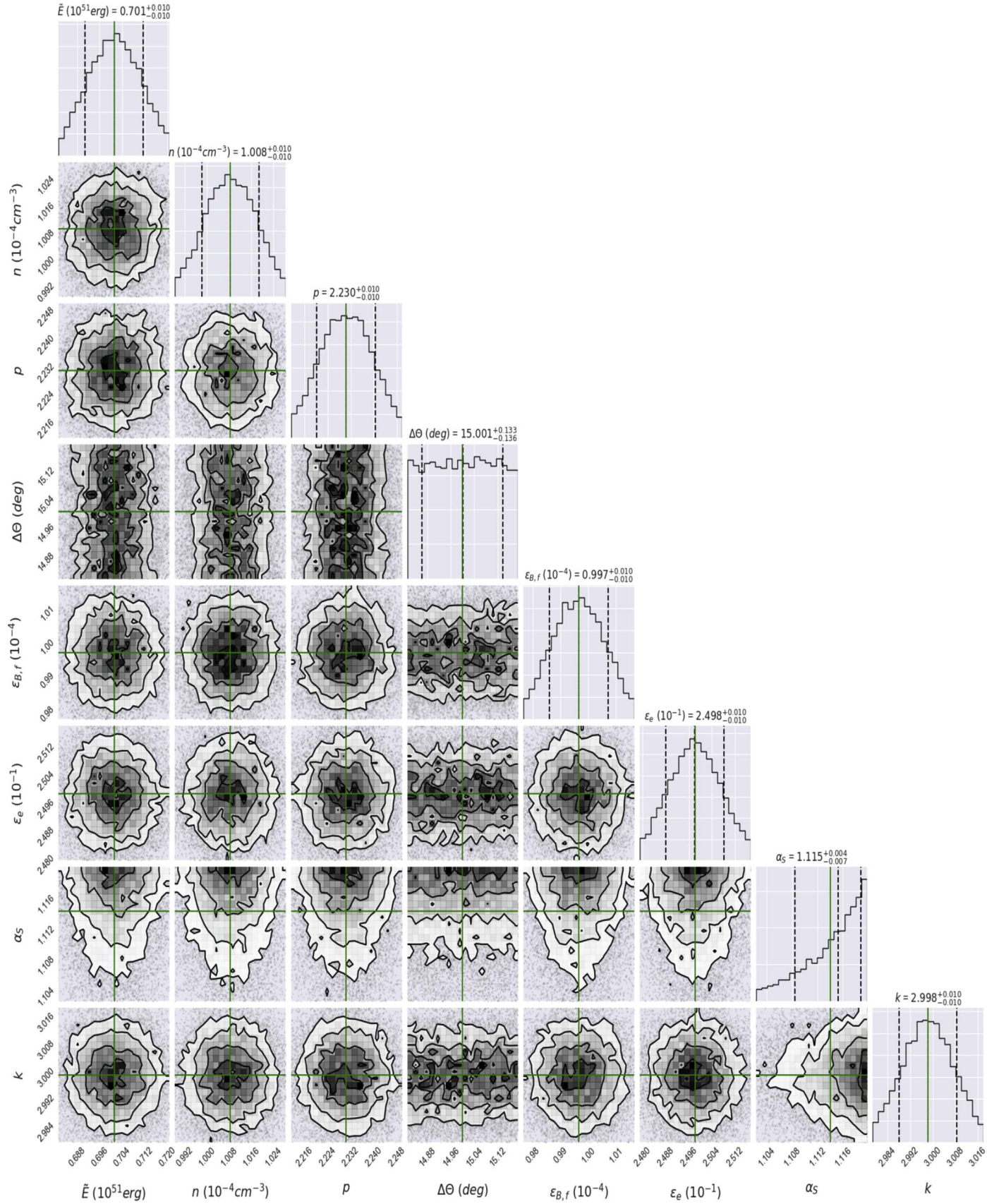

Figure 5. Same as Figure 2, but using a synchrotron forward-shock model to fit the X-ray data when the jet producing the afterglow emission is not aligned with the observer's line of sight and the matter in the outflow is parameterized through a power-law velocity distribution (model described in Section 2.2).

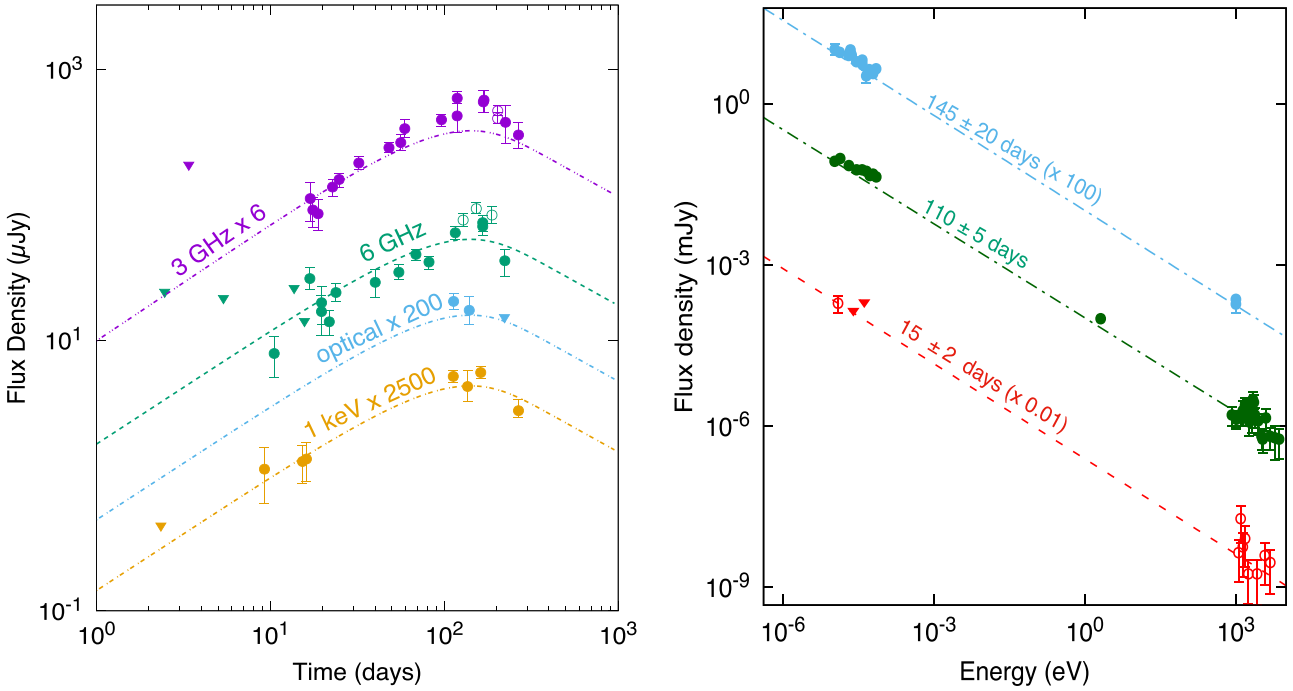

Figure 6. Right: SEDs of the X-ray, optical, and radio afterglow observations at 15 ± 2 (red), 110 ± 5 (green), and 145 ± 20 (blue) days. Left: light curves of X-rays at 1 keV (gold; Margutti et al. 2017a, 2017b, 2018; Troja et al. 2017a, 2017b, 2018; Haggard et al. 2018), optical (blue; Margutti et al. 2018), and radio at 3 and 6 GHz (magenta and green; Alexander et al. 2017; Hallinan et al. 2017; Mooley et al. 2017; Troja et al. 2017a) bands. The values that describe both the SED and the light curves are reported in Table 5.

3.3.2. Other Parameters

1. The values of the external medium densities required to model the γ-ray GBM data $\sim$1.7 s after the merger (see Table 3) and the X-ray, optical, and radio data (see Table 5) are quite different, indicating that the γ-ray emission and the afterglow occurred in different regions.This suggests that the external density distribution could be stratified, as proposed in sGRBs (Parsons et al. 2009). Binary NS mergers are thought to be potential candidates to eject significant masses with distinct velocities and densities. The ejected masses with densities larger than low ISM are ejected at sub-relativistic velocities. In principle, the ultra-relativistic jet coming out from the progenitor could interact with these dense material, producing an afterglow (Tan et al. 2001; Hotokezaka et al. 2013; Kyutoku et al. 2014; Hotokezaka & Piran 2015; Fraija et al. 2018). Moreover, fits to the multiwavelength afterglow have suggested that the circum-burst medium close to the progenitor could be dense and be formed by gaseous environments rather than the low ISM (Panaitescu 2006; Berger 2007; Nakar 2007; Nysewander et al. 2009; Parsons et al. 2009). The low value of the ISM would confirm that sGRBs explode in lower-density environments.
2. The values of the electron spectral indexes for the γ-ray flux and the X-ray, optical, and radio fluxes are equal. These spectral indexes correspond to the typical values reported in external shocks $2.2 \leqslant p \leqslant 2.6$ (e.g., see; Kumar & Zhang 2015). It suggests that the GBM γ-ray flux could have originated in external shocks. Similar results have been found in several bursts that have exhibited early sub-GeV γ-ray and optical peaks together with temporarily extended multiwavelength emissions (Kobayashi & Zhang 2007; Kobayashi et al. 2007; Fraija 2015; Fraija et al. 2016a, 2017b).
3. Two scenarios are discussed in order to explain GRB 170817A (e.g., Murguia-Berthier et al. 2017): a low-luminosity sGRB and a typical sGRB viewed off-axis. Whereas low-luminosity sGRBs could be produced by a mildly relativistic outflow (Rosswog & Ramirez-Ruiz 2002, 2003; Nagakura et al. 2014), a typical sGRB is generated by a relativistic jet (Ramirez-Ruiz et al. 2005; Murguia-Berthier et al. 2014). In both cases a relativistic jet is invoked; however, in the first case the jet is choked by the wind expelled from the hyper massive neutron star (HMNS), thus giving rise to a low-luminosity sGRB with $E_{\gamma,\rm iso} \simeq 10^{46}$–$10^{47}$ erg. Considering the values of the equivalent energy we estimate for this event (see Tables 3 and 5), we suggest that the most likely scenario for GRB 170817A is that of a jet that successfully breaks out from the wind and it is viewed off-axis. This result agrees with the recent work by Mooley et al. (2018), where authors present Very Long Baseline Interferometry observations that show superluminal motion and support the successful breakout of the jet.
4. The collimation of ejecta has relevant implications in GRBs, such as, for instance, the energy scale, the energy extraction mechanism and the event rate. For sGRBs, there are only a few observations of jet breaks despite serious search efforts. Based on the breaks detected in the afterglow emission, Berger (2014) showed a distribution of jet opening angles for sGRBs with a mean around $\theta_j \sim \langle 5^\circ \rangle$. Recently, a similar value of opening angle was obtained after modeling the afterglow in GRB 170817A (i.e., see; Granot et al. 2017; Troja et al. 2018). Taking into account the value of $\theta_j = 5^\circ$, the viewing angle for GRB 170817A would be $\theta_{\rm obs} = 20^\circ$, which is in the

range reported for this burst (Granot et al. 2017; Margutti et al. 2017a, 2018; Mooley et al. 2018; Troja et al. 2018).
5. Considering the values reported together with Equations (8) and (9), the bulk Lorentz factor is $\Gamma \simeq 8.7$ and the equivalent kinetic energy is $E_k \simeq 3.3 \times 10^{47}$ erg. Comparing with the observed isotropic energy $E_{\gamma,\rm iso} \simeq 5 \times 10^{46}$ erg, the corresponding efficiency becomes $\eta \simeq 15\%$, which lies in the typical range reported for afterglows (e.g., see; Kumar & Zhang 2015).

4. Conclusions

We have analyzed the non-thermal (γ-ray, X-ray, optical, and radio) observations of GRB 170817A/GW170817. The X-ray, optical, and radio data were consistent with the synchrotron forward-shock model when the jet is viewed off-axis and the matter in the outflow is parameterized through a power-law velocity distribution. The origin of the γ-ray peak was discussed in terms of internal and external shocks. The analysis performed favors a SSC reverse-shock model in the fast-cooling regime observed at high latitudes. The fit of the γ-ray GBM data with SSC model suggests that:

1. The circumburst medium close to the progenitor is much denser than the low ISM obtained after modeling the X-ray, optical, and radio data. One possible explanation is that the external density distribution could be stratified as proposed in sGRBs (Tan et al. 2001; Parsons et al. 2009; Hotokezaka et al. 2013; Kyutoku et al. 2014; Hotokezaka & Piran 2015; Fraija et al. 2018); the circumburst medium close to the progenitor could be formed by gaseous environments and/or dense ejected masses rather than a very low-density medium of the host galaxy. This suggests that the afterglow and γ-ray emission occurred in different regions.
2. The value of the electron spectral index illustrates that this component could have originated at the external shocks. Similar discussions have been previously reported around the temporarily extended Fermi-LAT components (Kobayashi & Zhang 2007; Kobayashi et al. 2007; Fraija 2015; Fraija et al. 2016a, 2017b).
3. The value of the magnetic microphysical parameter obtained agrees with the temporal properties exhibited by this burst and also indicates that the strength of the magnetic field is 3-4 orders of magnitude higher than usual strength in an NS $\sim 10^{12}$ G. By comparing the magnetic microphysical parameters obtained for γ-ray flux with the X-ray, optical, and radio observations is shown that the magnetic field in the reverse-shock region would be $\sim$40 times higher than the forward shock. This suggests that the outflow carried a significant magnetic field, as reported in sGRB 090510 (Fraija et al. 2016b).

The value of the equivalent kinetic energy agrees with simulations performed around the necessary conditions for sGRB production in binary NS mergers (Murguia-Berthier et al. 2014). This suggests that the scenario in which a collapse to a black hole occurs with the formation of a typical off-axis sGRB is favored when the wind expelled from HMNS hampers the forward movement of the on-axis jet.

Since GRB 170817A was the closest sGRB with measured redshift, it was proposed as a potential target for neutrino observation. However, the Antares, IceCube, and Auger observatories reported a null result based on a search during the prompt phase and afterglow (ANTARES et al. 2017; Bartos & IceCube Collaboration 2017). As shown in previous works (see i.e., Gao et al. 2013; Fraija et al. 2017b), the lack of energetic neutrinos around GRB 170817A could be related to the degree of ejecta magnetization, which hinders efficient particle acceleration (Sironi & Spitkovsky 2011).

One of the most energetic short bursts, GRB 090510 located at $z = 0.903$, was detected by *Fermi* and *Swift* (De Pasquale et al. 2010). This sGRB, seen on-axis, exhibited a short-lasting peak at the end of the prompt phase ($T_{90} = 0.3$ s) and a temporally extended component lasting hundreds of seconds. In addition, the Ultra Violet and Optical Telescope on board *Swift* started collecting optical data at 97 s after the initial trigger (Kuin & Hoversten 2009). The optical afterglow emission was described by a broken power law with the following best-fit parameters: an early decay slope of $-0.50^{+0.11}_{-0.13}$, a break time of $1.58^{+0.46}_{-0.37} \times 10^3$ s, a late decay slope of $1.13^{+0.11}_{-0.13}$, and a density flux of $\sim 10^{-13}$ erg cm^{-2} s^{-1}one day after the trigger. Fraija et al. (2016b) used an early-afterglow model to interpret the multi-wavelength light curve observations. In particular, SSC emission from the reverse shock was consistent with the bright LAT peak, provided that the progenitor was endowed with strong magnetic fields, thus associating this progenitor with a binary NS merger. The optical light curve was described by synchrotron forward-shock emission in the slow-cooling regime before and after the break time. A similar analysis for off-axis emission was done in this paper for GRB 170817A. The bright γ-ray peak was consistent with SSC radiation in the fast-cooling regime and the multiwavelength afterglow with synchrotron emission in the slow-cooling regime at different regions. Therefore, we argue that an amplification process related to the binary NS merger in GRB 170817A was present. This burst did not display high-energy photons (>100 MeV), probably due to the high charged particle background in the burst region (Kocevski & Fermi-LAT Collaboration 2017), the off-axis emission, and low isotropic energy.

Gravitational-wave observations from a binary NS merger associated with this GRB event (von Kienlin et al. 2017; Goldstein et al. 2017) cast the compact merger scenario in a new light. A similar analysis to the one presented here on future short GRBs could shed light on the nature of the progenitors, the evolution of the magnetic field, and the optical counterpart by addressing the short GRB-gravitational-wave association.

We thank the referee for a critical reading and significant suggestions that helped improve this manuscript. We also thank E. Ramirez-Ruiz for useful discussions. N.F. acknowledges financial support from UNAM-DGAPA-PAPIIT through grants IA102917 and IA102019. F.D.C. thanks the UNAM-PAPIIT grants IN117917 and support from the Miztli-UNAM supercomputer (project LANCAD-UNAM-DGTIC-281). P.V. thanks Fermi grants NNM11AA01A and 80NSSC17K0750. R.B.D. acknowledges support from the National Science Foundation under Grant 1816694. A.C.C.D.E.S.P. acknowledges that this study was financed in part by the Coordenação de Aperfeiçoamento de Pessoal de Nível Superior—Brasil (CAPES)—Finance Code 001 and also thanks the Professor Dr. C. G. Bernal for tutoring and useful discussions.

ORCID iDs

N. Fraija https://orcid.org/0000-0002-0173-6453
P. Veres https://orcid.org/0000-0002-2149-9846

References

Abbott, B. P., Abbott, R., Abbott, T. D., et al. 2017a, PhRvL, 119, 161101
Abbott, B. P., Abbott, R., Abbott, T. D., et al. 2017b, ApJL, 848, L12
Ackermann, M., Ajello, M., Asano, K., et al. 2013, ApJS, 209, 11
Alexander, K. D., Berger, E., Fong, W., et al. 2017, ApJL, 848, L21
Alexander, K. D., Margutti, R., Blanchard, P. K., et al. 2018, arXiv:1805.02870
ANTARES, IceCube, Auger, P., et al. 2017, arXiv:1710.05839
Barniol, D. R., Nakar, E., Piran, T., & Sari, R. 2015, MNRAS, 448, 417
Bartos, I. & IceCube Collaboration 2017, GCN, 21568
Berger, E. 2007, ApJ, 670, 1254
Berger, E. 2014, ARA&A, 52, 43
Blandford, R. D., & McKee, C. F. 1976, PhFl, 19, 1130
Bromberg, O., Tchekhovskoy, A., Gottlieb, O., Nakar, E., & Piran, T. 2017, arXiv:1710.05897
Brun, R., & Rademakers, F. 1997, NIMPA, 389, 81
Burrows, D. N., Romano, P., Falcone, A., et al. 2005, Sci, 309, 1833
Ciolfi, R., Kastaun, W., Giacomazzo, B., et al. 2017, PhRvD, 95, 063016
Coulter, D. A., Foley, R. J., Kilpatrick, C. D., et al. 2017, arXiv:1710.05452
D'Avanzo, P., Campana, S., Salafia, O. S., et al. 2018, arXiv:1801.06164
De Pasquale, M., Schady, P., & Kuin, N. P. M. 2010, ApJL, 709, L146
Derishev, E. V. 2007, Ap&SS, 309, 157
Dermer, C. D., Chiang, J., & Mitman, K. E. 2000, ApJ, 537, 785
Dobie, D., Kaplan, D. L., Murphy, T., et al. 2018, ApJL, 858, L15
Eichler, D., Livio, M., Piran, T., & Schramm, D. N. 1989, Natur, 340, 126
Fan, Y. Z., & Wei, D. M. 2005, MNRAS, 364, L42
Fan, Y. Z., Wei, D. M., & Wang, C. F. 2004, A&A, 424, 477
Foreman-Mackey, D. 2016, JOSS, 1, doi:10.21105/joss.00024
Fraija, N. 2015, ApJ, 804, 105
Fraija, N., Caligula do, A. C., Pedreira, E. S., & Veres, P. 2018, arXiv:1803.02978
Fraija, N., González, M. M., & Lee, W. H. 2012, ApJ, 751, 33
Fraija, N., Lee, W., & Veres, P. 2016a, ApJ, 818, 190
Fraija, N., Lee, W. H., Araya, M., et al. 2017a, ApJ, 848, 94
Fraija, N., Lee, W. H., Veres, P., & Barniol Duran, R. 2016b, ApJ, 831, 22
Fraija, N., & Veres, P. 2018, ApJ, 859, 70
Fraija, N., Veres, P., Zhang, B. B., et al. 2017b, ApJ, 848, 15
Gao, S., Kashiyama, K., & Mészáros, P. 2013, ApJL, 772, L4
Giacomazzo, B., Rezzolla, L., & Baiotti, L. 2009, MNRAS, 399, L164
Giblin, T. W., van Paradijs, J., Kouveliotou, C., et al. 1999, ApJL, 524, L47
Goldstein, A., Veres, P., Burns, E., et al. 2017, arXiv:1710.05446
Gottlieb, O., Nakar, E., Piran, T., & Hotokezaka, K. 2017, arXiv:1710.05896
Granot, J., Gill, R., Guetta, D., & De Colle, F. 2017, arXiv:1710.06421
Granot, J., Panaitescu, A., Kumar, P., & Woosley, S. E. 2002, ApJL, 570, L61
Guetta, D., Spada, M., & Waxman, E. 2001, ApJ, 557, 399
Guidorzi, C., Margutti, R., Brout, D., et al. 2017, arXiv:1710.06426
Haggard, D., Nynka, M., Ruan, J. J., Evans, P., & Kalogera, V. 2018, ATel, 11242
Hallinan, G., Corsi, A., Mooley, K. P., et al. 2017, arXiv:1710.05435
Hotokezaka, K., Kyutoku, K., Tanaka, M., et al. 2013, ApJL, 778, L16
Hotokezaka, K., & Piran, T. 2015, MNRAS, 450, 1430
Ioka, K., & Nakamura, T. 2017, arXiv:1710.05905
Just, O., Obergaulinger, M., Janka, H.-T., Bauswein, A., & Schwarz, N. 2016, ApJL, 816, L30
Kasen, D., Badnell, N. R., & Barnes, J. 2013, ApJ, 774, 25
Kasliwal, M. M., Nakar, E., Singer, L. P., et al. 2017, Sci, 358, 1559
Kathirgamaraju, A., Barniol Duran, R., & Giannios, D. 2017, arXiv:1708.07488
Kathirgamaraju, A., Tchekhovskoy, A., Giannios, D., & Barniol Duran, R. 2018, arXiv:1809.05099
Kisaka, S., Ioka, K., Kashiyama, K., & Nakamura, T. 2017, arXiv:1711.00243
Kobayashi, S. 2000, ApJ, 545, 807
Kobayashi, S., Piran, T., & Sari, R. 1997, ApJ, 490, 92
Kobayashi, S., & Zhang, B. 2003, ApJ, 597, 455
Kobayashi, S., & Zhang, B. 2007, ApJ, 655, 973
Kobayashi, S., Zhang, B., Mészáros, P., & Burrows, D. 2007, ApJ, 655, 391
Kocevski, D. & Fermi-LAT Collaboration 2017, GCN, 21534
Kuin, N. P. M., & Hoversten, E. A. 2009, GCN, 9342, 1
Kumar, P., & Panaitescu, A. 2000, ApJL, 541, L51
Kumar, P., & Panaitescu, A. 2003, MNRAS, 346, 905
Kumar, P., & Zhang, B. 2015, PhR, 561, 1
Kyutoku, K., Ioka, K., & Shibata, M. 2014, MNRAS, 437, L6
Lattimer, J. M., & Schramm, D. N. 1974, ApJL, 192, L145
Lattimer, J. M., & Schramm, D. N. 1976, ApJ, 210, 549
Lazzati, D., Deich, A., Morsony, B. J., & Workman, J. C. 2017a, MNRAS, 471, 1652
Lazzati, D., López-Cámara, D., Cantiello, M., et al. 2017b, ApJL, 848, L6
Lazzati, D., Perna, R., Morsony, B. J., et al. 2017c, arXiv:1712.03237
Lee, W. H., & Ramirez-Ruiz, E. 2007, NJPh, 9, 17
Lee, W. H., Ramirez-Ruiz, E., & Page, D. 2004, ApJL, 608, L5
Lee, W. H., Ramirez-Ruiz, E., & Page, D. 2005, ApJ, 632, 421
Li, L.-X., & Paczyński, B. 1998, ApJL, 507, L59
Lu, R.-J., Hou, S.-J., & Liang, E.-W. 2010, ApJ, 720, 1146
Lyman, J. D., Lamb, G. P., Levan, A. J., et al. 2018, arXiv:1801.02669
Margutti, R., Alexander, K. D., Xie, X., et al. 2018, arXiv:1801.03531
Margutti, R., Berger, E., Fong, W., et al. 2017a, ApJL, 848, L20
Margutti, R., Fong, W., Eftekhari, T., et al. 2017b, ATel, 11037
McMahon, E., Kumar, P., & Panaitescu, A. 2004, MNRAS, 354, 915
McMahon, E., Kumar, P., & Piran, T. 2006, MNRAS, 366, 575
Mészáros, P. 2006, RPPh, 69, 2259
Metzger, B. D. 2017, LRR, 20, 3
Metzger, B. D., Martínez-Pinedo, G., Darbha, S., et al. 2010, MNRAS, 406, 2650
Mimica, P., Giannios, D., & Aloy, M. A. 2009, A&A, 494, 879
Mimica, P., Giannios, D., & Aloy, M. A. 2010, MNRAS, 407, 2501
Mooley, K. P., Deller, A. T., Gottlieb, O., et al. 2018, arXiv:1806.09693
Mooley, K. P., Nakar, E., Hotokezaka, K., et al. 2017, arXiv:1711.11573
Mundell, C. G., Kopač, D., Arnold, D. M., et al. 2013, Natur, 504, 119
Mundell, C. G., Steele, I. A., Smith, R. J., et al. 2007, Sci, 315, 1822
Murguia-Berthier, A., Montes, G., Ramirez-Ruiz, E., De Colle, F., & Lee, W. H. 2014, ApJL, 788, L8
Murguia-Berthier, A., Ramirez-Ruiz, E., Kilpatrick, C. D., et al. 2017, ApJL, 848, L34
Nagakura, H., Hotokezaka, K., Sekiguchi, Y., Shibata, M., & Ioka, K. 2014, ApJL, 784, L28
Nakar, E. 2007, PhR, 442, 166
Nakar, E., & Piran, T. 2004, MNRAS, 353, 647
Nakar, E., & Piran, T. 2011, Natur, 478, 82
Nakar, E., Piran, T., & Granot, J. 2002, ApJ, 579, 699
Narayan, R., Paczynski, B., & Piran, T. 1992, ApJL, 395, L83
Nysewander, M., Fruchter, A. S., & Pe'er, A. 2009, ApJ, 701, 824
O'Brien, P. T., Willingale, R., Osborne, J., et al. 2006, ApJ, 647, 1213
Obergaulinger, M., Aloy, M. A., & Müller, E. 2010, A&A, 515, A30
Panaitescu, A. 2006, MNRAS, 367, L42
Panaitescu, A. 2007, MNRAS, 379, 331
Parsons, R. K., Ramirez-Ruiz, E., & Lee, W. H. 2009, arXiv:0904.1768
Peng, Z. Y., Ma, L., Zhao, X. H., et al. 2009, ApJ, 698, 417
Piran, T. 1999, PhR, 314, 575
Piran, T., Nakar, E., & Rosswog, S. 2013, MNRAS, 430, 2121
Piro, A. L., & Kollmeier, J. A. 2017, arXiv:1710.05822
Price, D. J., & Rosswog, S. 2006, Sci, 312, 719
Ramirez-Ruiz, E., Granot, J., Kouveliotou, C., et al. 2005, ApJL, 625, L91
Rees, M. J. 1999, A&AS, 138, 491
Rees, M. J., & Meszaros, P. 1994, ApJL, 430, L93
Rosswog, S. 2005, ApJ, 634, 1202
Rosswog, S., & Ramirez-Ruiz, E. 2002, MNRAS, 336, L7
Rosswog, S., & Ramirez-Ruiz, E. 2003, MNRAS, 343, L36
Salvatier, J., Wieckiâ, T. V., & Fonnesbeck, C. 2016, PyMC3: Python probabilistic programming framework, Astrophysics Source Code Library, ascl:1610.016
Sari, R. 1997, ApJL, 489, L37
Sari, R., & Mészáros, P. 2000, ApJL, 535, L33
Sari, R., & Piran, T. 1995, ApJL, 455, L143
Sari, R., Piran, T., & Halpern, J. P. 1999, ApJL, 519, L17
Sari, R., Piran, T., & Narayan, R. 1998, ApJL, 497, L17
Sironi, L., & Spitkovsky, A. 2011, ApJ, 726, 75
Spergel, D. N., Verde, L., Peiris, H. V., et al. 2003, ApJS, 148, 175
Steele, I. A., Mundell, C. G., Smith, R. J., Kobayashi, S., & Guidorzi, C. 2009, Natur, 462, 767
Tan, J. C., Matzner, C. D., & McKee, C. F. 2001, ApJ, 551, 946
Troja, E., Lipunov, V. M., Mundell, C. G., et al. 2017a, Natur, 547, 425
Troja, E., Piro, L., Ryan, G., et al. 2018, arXiv:1801.06516
Troja, E., Piro, L., van Eerten, H., et al. 2017b, Natur, 000, 1
Usov, V. V. 1992, Natur, 357, 472
Veres, P., Mészáros, P., Goldstein, A., et al. 2018, arXiv:1802.07328
Vestrand, W. T., Wren, J. A., Wozniak, P. R., et al. 2006, Natur, 442, 172
von Kienlin, A., Meegan, C., & Goldstein, A. 2017, GCN, 21520
Wang, X.-Y., & Huang, Z.-Q. 2018, ApJL, 853, L13
Zhang, B., Fan, Y. Z., Dyks, J., et al. 2006, ApJ, 642, 354
Zhang, B., & Kobayashi, S. 2005, ApJ, 628, 315
Zhang, B., Kobayashi, S., & Mészáros, P. 2003, ApJ, 595, 950
Zhang, B., & Mészáros, P. 2004, IJMPA, 19, 2385
Zrake, J., & MacFadyen, A. I. 2013, ApJL, 769, L29